

Article

Lattice Distortion in $\text{Co}_3\text{O}_4/\text{Mn}_3\text{O}_4$ -Guided Synthesis via Carbon Nanotubes for Efficient Lean Methane Combustion

Xinfang Wei ^{1,*}, Ke Yang ¹, Qinghan Zhu ¹, Jinlong Li ¹, Jian Qi ^{2,3,*}  and Haiwang Wang ^{1,*}

¹ Key Laboratory of Dielectric and Electrolyte Functional Material Hebei Province, Northeastern University at Qinhuangdao, Qinhuangdao 066004, China; y1210620501@163.com (K.Y.); zhuqinghan0110@163.com (Q.Z.); lj1218126@126.com (J.L.)

² State Key Laboratory of Biochemical Engineering, Institute of Process Engineering, Chinese Academy of Sciences, Beijing 100190, China

³ School of Chemical Engineering, University of Chinese Academy of Sciences, Beijing 100049, China

* Correspondence: weixinfang@neuq.edu.cn (X.W.); jqj@ipe.ac.cn (J.Q.); whwdbdx@neuq.edu.cn (H.W.)

Abstract: In this paper, with the synergistic effect of C, Co and O elements, and with a one-dimensional carbon nanotube (CNT) as the structure guide agent, a two-dimensional Co_3O_4 nano-sheet with high catalytic activity was prepared, and its catalytic activity was further improved by adding a manganese element. By controlling the annealing time, a two-dimensional Co_3O_4 -based nano-sheet with a regular arrangement of atoms on the surface was gradually formed during the oxidation process of CNT. Then, the lattice distortion of Co_3O_4 was caused by doping manganese. The interaction between Mn and Co promotes the cycle capacity of Mn/Co redox pair and the generation of reactive oxygen species, which is conducive to an improvement in catalytic activity. Finally, under different catalytic conditions, the 2D Co_3O_4 -based catalysts all showed stable catalytic performances, among which methane flow rate had a great influence. When the airspeed was controlled within the range of $42,000 \text{ mL}\cdot\text{g}^{-1}\cdot\text{h}^{-1}$, the methane conversion rate could still reach 90% (450°C).

Keywords: lattice distortion; $\text{Co}_3\text{O}_4/\text{Mn}_3\text{O}_4$; carbon nanotube; structure guide agent; lean methane combustion



Citation: Wei, X.; Yang, K.; Zhu, Q.;

Li, J.; Qi, J.; Wang, H. Lattice

Distortion in $\text{Co}_3\text{O}_4/\text{Mn}_3\text{O}_4$ -Guided Synthesis via Carbon Nanotubes for Efficient Lean Methane Combustion.

Catalysts **2023**, *13*, 1112. <https://doi.org/10.3390/catal13071112>

Academic Editors: Mingjun Jia and Xintong Zhang

Received: 10 May 2023

Revised: 7 July 2023

Accepted: 13 July 2023

Published: 17 July 2023



Copyright: © 2023 by the authors. Licensee MDPI, Basel, Switzerland. This article is an open access article distributed under the terms and conditions of the Creative Commons Attribution (CC BY) license (<https://creativecommons.org/licenses/by/4.0/>).

1. Introduction

In coal mining, gas turbines, and other industrial applications, there are many methane emissions, and the traditional high-temperature incineration method leads to secondary pollution, so the realization of efficient methane conversion has become a problem to be solved [1]. With the increasing demand for sustainable energy and green energy, the use of catalysts to catalyze methane is an efficient and effective way to purify waste gas. It is well known that spinel-phase Co_3O_4 can catalyze the deep oxidation of low concentration methane, which is considered as one of the most promising transition oxide catalysts [2–4]. Studies have shown that a Co_3O_4 catalyst can give full play to the size effect, the nanometer size of which can further improve the catalytic activity [5–7]. Moreover, even with nanocrystalline catalysts of the same size, the catalytic efficiency of methane is still greatly different due to their different morphologies [8–12]. This is mainly due to the different arrangement of atoms on the surface of catalysts with different morphologies, which leads to great differences in the number of dangling bonds on the crystal surface and the content of vacancy oxygen on the surface and, finally, affects the catalytic activity [13]. Among the various common nano-topologies, the two-dimensional oriented Co_3O_4 nano-catalyst has unique catalytic properties due to its large specific surface area, regular atomic arrangement on the surface and large number of dangling bonds [14,15].

Therefore, the design and preparation of Co_3O_4 nanomaterials with special morphology, and their alloys, have attracted wide attention [16]. Yang et al. developed the aqueous phase extraction method to prepare nanometer quantum dots and their alloys [17], which

have very regular microstructures and excellent catalytic properties. Hu et al. prepared a two-dimensional flaky Co_3O_4 catalyst with an exposed {112} crystal surface using the hydrothermal method and realized the complete catalysis of low-concentration methane (2% CH_4 + 98% air) under the temperature of 375 °C [13]. Also, they prepared two-dimensional Co_3O_4 nano-sheets with high species content of surface oxygen using the hydrothermal method [15], which can completely catalyze methane gas (1.6% CH_4 + 7.0% O_2 + 91.4% N_2) at 473 °C. Chen et al. also successfully prepared a two-dimensional hexagon Co_3O_4 catalyst with an exposed {111} crystal surface using the hydrothermal method and achieved 100% methane conversion (0.2% CH_4 + 99.8% air) at 500 °C [10].

In recent years, studies have shown that, under the synergistic effect of elements, not only can new materials with unique structure be prepared, but novel materials with excellent performance can also be prepared [18–20]. Research has shown that the composite material obtained by combining transition metal oxides with Co_3O_4 can combine the advantages of different substances. It has better electrochemical performance when used as an anode of a lithium battery [21–23]. In 2010, Song et al. found that metal sheets loaded inside the CNT could diffuse to the position of carbon atoms inside the CNT under thermal oxidation, thus forming metal oxide nanotubes [24]. The metal/metal oxide CNT nanotubes and mesoporous metal oxide nanotubes are expected to find many applications, such as in lithium ion batteries, catalysis, magnetic drug delivery and gas sensing [25]. In 2017, Bol et al. successfully prepared single-walled CNT, using Co_3O_4 film as the substrate, through reduction, vapor deposition and other processes [26]. In this process, Co acts as a catalyst, and the CNT prepared by this process have the characteristics of good regularity and strong controllability [27,28].

In this work, the 2D Co_3O_4 nano-sheet catalyst, and its $\text{Co}_3\text{O}_4/\text{Mn}_3\text{O}_4$ composite oxide with lattice distortion were prepared by using 1D CNT as the structure guide and under the coordination of C, O and Co elements. This kind of material had a simple preparation process, novel microstructure and an excellent catalytic oxidation performance of methane, which was tested on a fixed-bed evaluation device (Figure S1) and provided a new method for the design and preparation of new Co_3O_4 -based nanomaterials [29].

2. Results

2.1. Structural Properties of Co_3O_4 Nano-Sheet

Figure 1 is the transmission electron microscope (TEM) image of CNT and the two-dimensional Co_3O_4 nano-sheet (the preparation method is shown in Section 4.1). In Figure 1a, 0.34 nm is the corresponding (002) crystal surface. In Figure 1b, the diameter of CNT is about 20 nm. In Figure 1c, 0.46 nm and 0.24 nm, respectively, corresponded to the (111) and (311) crystal surfaces of Co_3O_4 , mainly based on the (111) crystal plane, which means that the atomic arrangement of the exposed crystal plane of Co_3O_4 is relatively regular. According to Figure 1d, the diameter and size of the Co_3O_4 nano-sheet can be further determined to be about 20 nm, close to the diameter of CNT [30].

The TG diagram of CNT, $\text{Co}(\text{NO}_3)_2 \cdot 6\text{H}_2\text{O}$ and Co_3O_4 nanometer sheet precursors in the air atmosphere are shown in Figure 2a. Among them, the CNT begins to be oxidized at about 500 °C and is completely oxidized at about 650 °C. $\text{Co}(\text{NO}_3)_2 \cdot 6\text{H}_2\text{O}$ began to be oxidized at about 100 °C, and is completely oxidized at about 300 °C. The TG curve of the precursor of Co_3O_4 nano-sheet indicates that, as cobalt nitrate is decomposed and part of the cobalt is oxidized to Co_3O_4 , the ratio of the Co^{3+} and Co^{2+} content in the sample is 0.79, the oxidation temperature of CNT decreased and it can be completely oxidized at about 500 °C; the existence of Co_3O_4 prompted the complete oxidation of CNT nearly 200 °C in advance. The pore size distribution diagram of CNT and the Co_3O_4 nano-sheet (Figure 2b) indicates that the sample of the Co_3O_4 nano-sheet has a wide range of pore sizes, which is significantly different from the pore volume of CNT and has a large difference in specific surface area. The BET characterization data of the two samples are given in Table 1.

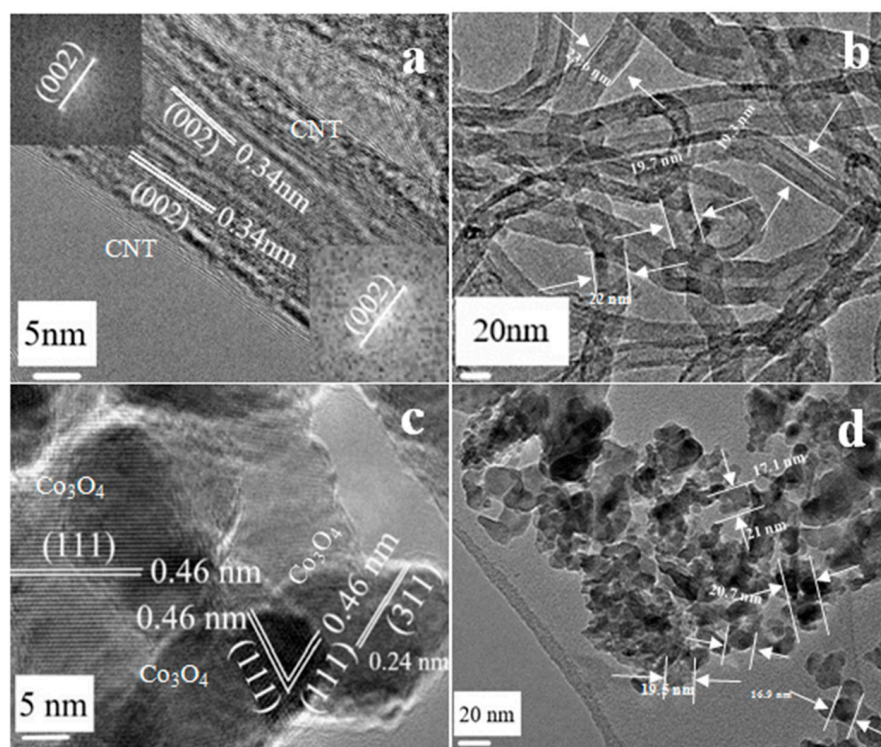


Figure 1. (a) HRTEM images of CNT; (b) TEM images of CNT; (c) HRTEM images of Co_3O_4 nano-sheet; (d) TEM images of Co_3O_4 nano-sheet.

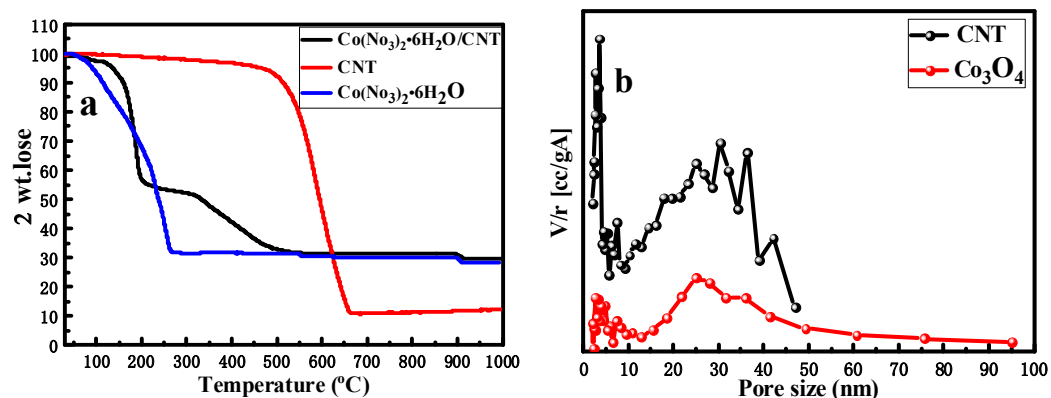


Figure 2. (a) TG patterns of $\text{Co}(\text{NO}_3)_2 \cdot 6\text{H}_2\text{O}$, CNT and $\text{Co}(\text{NO}_3)_2 \cdot 6\text{H}_2\text{O}/\text{CNT}$; (b) pore size distributions of Co_3O_4 nano-sheet and CNT.

Table 1. Pore parameters of different catalysts.

Sample	Average Pore Size (nm)	Surface Area (m^2g^{-1})	Total Pore Volume (cm^3g^{-1})
CNT	16.12	128.51	0.52
Co_3O_4	34.16	28.50	0.24
Co _{0.9} /Mn _{0.5}	24.70	64.81	0.44
Mn _{0.5} /CNT	25.28	144.34	0.77

2.2. Analysis of the Formation Process of Co_3O_4 Nano-Sheet

It has been observed that Co_3O_4 has a significant effect on the stability of CNT through the characterization analysis in Figure 2. The influence of Co_3O_4 on the thermochemical stability of CNT is also an important reason for the formation of two-dimensional Co_3O_4

nano-sheets, so the influence of Co_3O_4 on the oxidation behavior of CNT was analyzed in detail [31].

To help further understand the effect of Co_3O_4 on the oxidation of CNTs, we annealed the CNT samples that were loaded with cobalt nitrate at 400°C for different times (1 min, 3 min, 6 min, 10 min, 30 min and 60 min), and four samples (1 min, 6 min, 30 min and 60 min) were selected for detailed characterization analysis. Figure 3a–d are SEM diagrams of the four samples. It can be found that the structure of CNT changes significantly with the passing of time, that is, CNT changes from the initial tubular structure to the spherical structure assembled by the two-dimensional nano-sheet. The change in structure indicates that the oxidation degree of CNT increases gradually. SEM diagrams of other samples are shown in Figure S2.

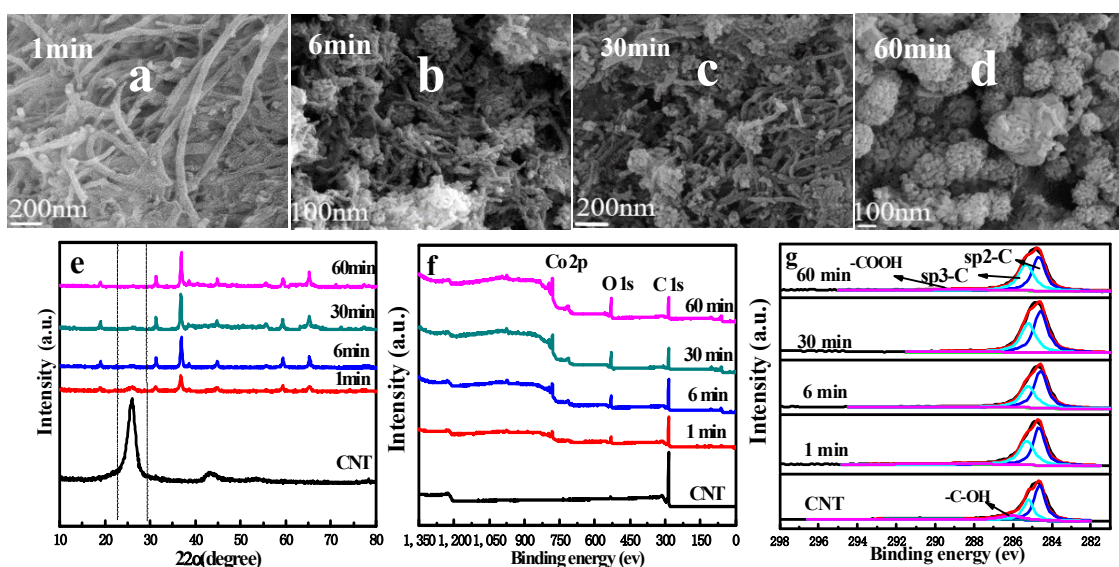


Figure 3. (a–d) SEM images of Co_3O_4 nano-sheet prepared at different holding times; (e) XRD patterns of Co_3O_4 nano-sheet prepared at different annealing times; (f) X-ray photoelectron spectrum of Co_3O_4 nano-sheet prepared at different annealing times; (g) peak deconvolutions of C 1s core lines in XPS spectra of Co_3O_4 nano-sheet prepared at different annealing times.

The XRD characterization of the four samples is shown in Figure 3e. The diffraction peaks of Co_3O_4 nano-sheet samples well fit the data of the plane diffraction standard of the cubic spinel Co_3O_4 (111), (220), (311), (222), (400), (422), (511) and (440), and no CNT diffraction peaks were observed. The diffraction peak of CNT gradually weakened, and the diffraction peak of the sample was completely consistent with that of the structure of the spinel Co_3O_4 (JCPDS NO: 76-1802) after 60 min of air burning, further indicating the transition oxidation of CNT. The XRD diagrams of the remaining samples are shown in Figure S3.

Figure 3f shows the full spectrum of XPS of the four samples. Even after 60 min of air burning, the presence of higher contents of carbon elements can still be found, which is attributed to the existence of more stable carbon impurities in the oxidation process. The atomic mass percentages of the three elements, Co, O and C, are given in Table 2, where the content of C gradually decreases with the extension of the blanking time, and the elements Co and O show an opposite trend, which is consistent with the trend of SEM and XPS full spectrum. The carbon bonds of carbon elements in different samples were mainly sp^2 -hybridization bonds and sp^3 -hybridization bonds, and the carbon peak of the initial CNT was mainly sp^2 -hybridization. In Figure 3g, the sp^3 -hybridization degree gradually increases with the extension of the air burning time, indicating that the stability of CNT gradually deteriorates, and the degree of oxidation gradually deepens [32]. However, two-dimensional Co_3O_4 nano-sheets are gradually formed along with the change in CNT

structure, which proves that sufficient air burning time is an important prerequisite for the formation of Co_3O_4 nano-sheets.

Table 2. XPS Results of CNT and Co_3O_4 nano-sheet catalysts prepared at different holding times (surface atomic composition (%), peak position (eV)).

Sample	Surface Atomic Composition (%)			Peak Position (eV)
	Co	O	C	C 1s
60 min	9.62	26.31	64.07	284.8
30 min	7.31	23.56	69.12	284.8
6 min	4.82	15.04	80.14	284.6
1 min	2.99	10.33	86.68	284.8
CNT	-	2.31	97.69	284.8

2.3. Structural Properties of Mn0.5/CNT and Co0.9/Mn0.5 Nano-Sheets

Recent studies have shown that Co-Mn composite oxide catalysts have higher catalytic activity [33]. Li et al. reported that Co_5Mn_1 catalysts prepared by co-precipitation processes have higher catalytic activity on methane combustion than pure Co_3O_4 [34]. Tian et al. reported that there was a good synergistic effect between Co_3O_4 and MnO_2 , which promoted the formation of reactive oxygen species by changing the lattice structure of Co_3O_4 [35]. Marco et al. also reported the following reactivity trends observed in total oxidation of VOCs: $\text{Mn}_3\text{O}_4 > \text{Mn}_2\text{O}_3 > \text{Mn}_x\text{O}_y$ [36]. This indicates that the synergistic effect between Co_3O_4 and oxygen species with different valence manganese can not only optimize the structure of the catalyst, but also improve the catalytic performance. However, the preparation of a 2D nano-structure co-manganese composite catalyst for methane oxidation has not been reported.

Here, on the basis of the preparation process of Co_3O_4 nano-sheet catalysts, different proportions of manganese oxides were further added, and the optimal amount of manganese oxides was determined by preparing MnO_2/CNT with different manganese loads. In Figure S4a, the catalytic activities of $\text{Mn}_{0.7}/\text{CNT}$ and $\text{Mn}_{0.5}/\text{CNT}$ were not significantly different, so the concentration of manganese nitrate was determined to be 0.5 M.

Figure 4 shows the TEM images of $\text{Mn}_{0.5}/\text{CNT}$ and $\text{Co}_{0.9}/\text{Mn}_{0.5}$ samples. In the HRTEM diagram of the $\text{Mn}_{0.5}/\text{CNT}$ catalyst (Figure 4a), the crystal plane spacing of 0.34 nm corresponds to the (002) crystal plane of CNT and the crystal plane spacing of 0.31 nm corresponds to the (110) crystal plane of MnO_2 . In Figure 4b, the tubular structure of CNT was retained in the sample of $\text{Mn}_{0.5}/\text{CNT}$, and the sheet size of MnO_2 was within the range of 25~40 nm around the CNT in the form of nanosheets. Figure 4c,d show HRTEM and TEM diagrams of $\text{Co}_{0.9}/\text{Mn}_{0.5}$. According to Figure 4c, compared with the $\text{Co}_3\text{O}_4/\text{CNT}$ catalyst, the crystal lattice fringes of the $\text{Co}_{0.9}/\text{Mn}_{0.5}$ sample catalyst were fuzzy, with poor crystallinity and increased crystal plane spacing. Among them, the crystal plane spacing corresponding to Co_3O_4 (111) increased to 0.47 nm, indicating that the intervention of manganese ions caused lattice distortion of Co_3O_4 [37]. In Figure 4d, the morphology of $\text{Co}_{0.9}/\text{Mn}_{0.5}$ sample and Co_3O_4 nano-sheet is consistent, and the morphology is still a two-dimensional nano-sheet. The diameter and size of nano-sheets are about 20 nm, but the dispersion is better.

As above, we continued to collect characterization data for the SEM, XRD, XPS, TG and pore size distribution of $\text{Mn}_{0.5}/\text{CNT}$ and $\text{Co}_{0.9}/\text{Mn}_{0.5}$ samples. The SEM and EDS of the MnO_2/CNT and $\text{Co}_3\text{O}_4/\text{Mn}_3\text{O}_4$ samples are given in Figures S5 and S6. It can be seen in Figure S5 that the tubular morphology of the MnO_2/CNT catalyst with different manganese loads changed little, while the morphology of the $\text{Co}_3\text{O}_4/\text{Mn}_3\text{O}_4$ catalyst with different cobalt manganese ratios changed significantly. When Mn: Co = 5:1, the tubular shape of CNT begins to change. When Mn: Co = 1:1, the tubular structure completely

disappears, showing irregular sheets. When Mn: Co = 5:9, the appearance is as shown in Figure 4d.

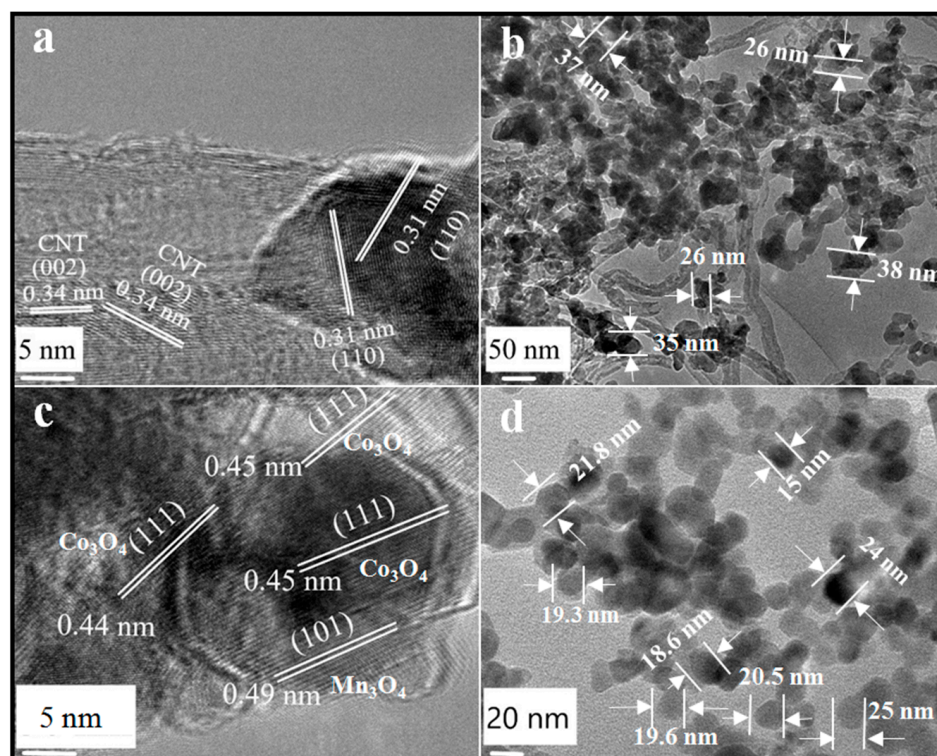


Figure 4. (a) HRTEM images of Mn0.5/CNT; (b) TEM images of Mn0.5/CNT; (c) HRTEM images of Co0.9/Mn0.5 nano-sheet; (d) TEM images of Co0.9/Mn0.5 nano-sheet.

In Figure S6, the content distribution of manganese and cobalt is positively correlated with the concentration of manganese salt and cobalt salt, which indicates that, before annealing, the adsorption amount of CNT on manganese salt and cobalt salt is proportional to the concentration of salt solution, and the load capacity is good.

In Figure 5a, the diffraction peaks of Mn0.5/CNT samples were shown as the composite peaks of CNT and MnO₂, while the diffraction peaks of Co0.9/Mn0.5 samples were highly consistent with those of the Co₃O₄ nano-sheet, and no peaks of CNT and Mn₃O₄ were observed. According to Figure S7a, the diffraction peaks of MnO₂/CNT catalysts with different manganese concentrations are consistent, and there is a change in peak strength which depends on the agglomeration degree of MnO₂. In Figure S7b, when the content of Co₃O₄ is low, the peak of Mn₃O₄ is obvious, but still has a strong oxidation effect on CNT, so the peak of CNT is not obvious. When Co₃O₄ content is high, there is no Mn₃O₄ diffraction peak, indicating that Mn₃O₄ is highly dispersed or partly exists in the lattice of Co₃O₄ in an amorphous form [34,38]. It is worth noting that, with the increase in cobalt salt concentration, the half-peak width of the diffraction peak of Co₃O₄ gradually widens, and the diffraction peak slightly shifts to the left, which indicates that part of Mn⁴⁺ is dispersed in the lattice of Co₃O₄. Replacing cobalt ions with manganese ions caused lattice distortion of Co₃O₄ and increased crystal plane spacing of Co₃O₄ [39], which was consistent with the HRTEM analysis results. From the perspective of crystal structure, the crystal field stability of Mn³⁺ is higher than that of Co³⁺ in octahedrons [34], so Mn³⁺ takes the place of Co³⁺ in octahedrons of spinel structure, where the Mn³⁺ ionic radius (0.066 nm) > the Co³⁺ ionic radius (0.065 nm) [35].

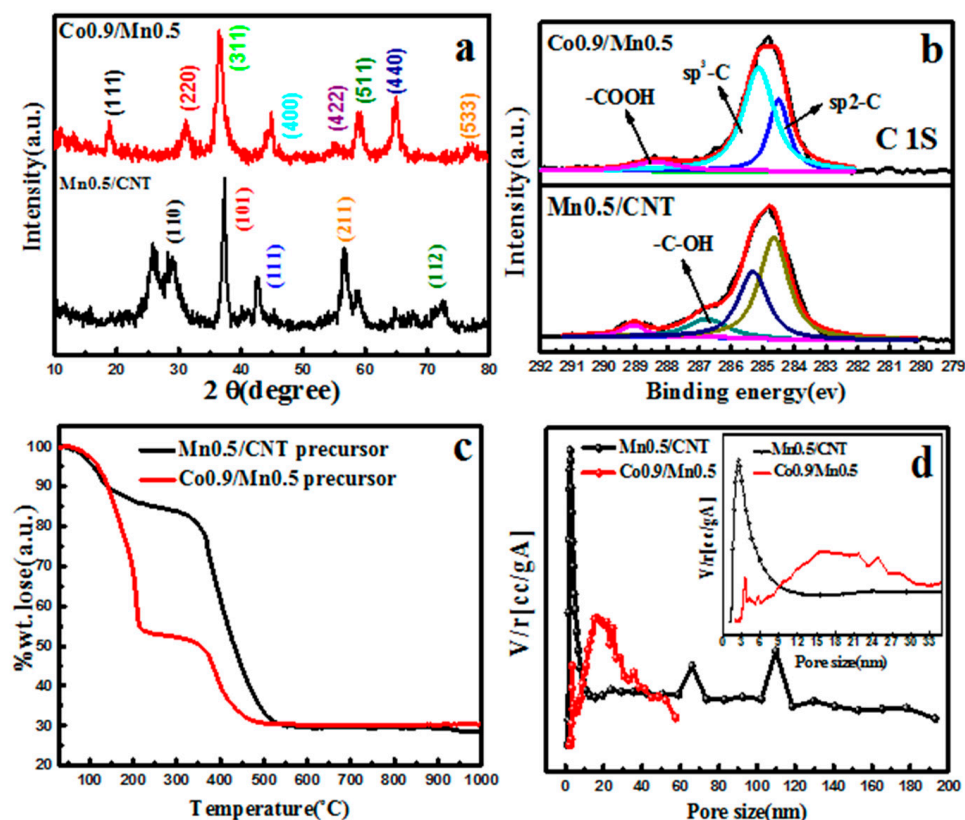


Figure 5. (a) XRD patterns of Mn_{0.5}/CNT and Co_{0.9}/Mn_{0.5} nano-sheet; (b) XPS spectra of C 1s acquired over Mn_{0.5}/CNT and Co_{0.9}/Mn_{0.5} nano-sheet; (c) TG patterns of Mn_{0.5}/CNT and Co_{0.9}/Mn_{0.5} nano-sheet precursor; (d) pore size distributions of Mn_{0.5}/CNT and Co_{0.9}/Mn_{0.5} nano-sheet.

Figure 5b shows the XPS spectra of the two samples, and it can be clearly observed that, compared with Mn_{0.5}/CNT, the sp³-hybridized carbon of Co_{0.9}/Mn_{0.5} sample is more obvious, and there is no -C-OH, indicating that the CNT oxidation in the Co_{0.9}/Mn_{0.5} sample is more serious. Figure 5c shows the TG diagram of the precursor Mn_{0.5}/CNT and Co_{0.9}/Mn_{0.5} in the air atmosphere. Among them, the completely weightlessness of CNT and manganese nitrate is at about 550 °C, and the TG curves of Co_{0.9}/Mn_{0.5} precursor is basically the same with the Co₃O₄ precursor. The pore size distribution diagram of MnO₂/CNT and Co₃O₄/Mn₃O₄ (Figure 5d) indicates that MnO₂/CNT has a large pore volume and a small pore size range, which may be related to the existence of good tubular CNT. The pore volume of Co_{0.9}/Mn_{0.5} is small and the pore diameter range is large, but the microscopic pore structure is better than that of the Co₃O₄ nano-sheet, so it has a larger specific surface area and pore volume. The pore size distribution and BET characterization data of MnO₂/CNT and Co₃O₄/Mn₃O₄ with different concentration variables are shown in Figure S8 and Table S1.

2.4. Activity Evaluation of Catalyst Oxidation of Methane

2.4.1. Catalytic Performance Test of Different Catalysts

So as to evaluate the catalytic activity of the Co₃O₄ nano-sheet, Co_{0.9}/Mn_{0.5} and Mn_{0.5}/CNT catalysts, methane conversion rates were tested at different temperatures ranging from 200 °C to 550 °C. As expected, the Co₃O₄ nano-sheet exhibited high catalytic activity, 98% of the methane combustion at 400 °C was implemented and, within the range of 250–350 °C, the methane combustion rate was faster.

Compared with the test results of the Co₃O₄ nano-sheet, the Co_{0.9}/Mn_{0.5} nano-sheet catalyst showed a higher methane combustion conversion rate (Figure 6), and 99% of methane combustion was achieved at 400 °C. The Co_{0.9}/Mn_{0.5} nano-sheet catalyst began

to catalyze methane combustion (3%) at 200 °C. This confirms that the addition of Mn can significantly improve the catalytic activity [40]. Compared with the Co_3O_4 nano-sheet at the same temperature, at 250 °C and 350 °C, the combustion of methane conversion was 10% higher. However, the Mn0.5/CNT catalyst showed lower activity, even though its specific surface area and pore volume were larger.

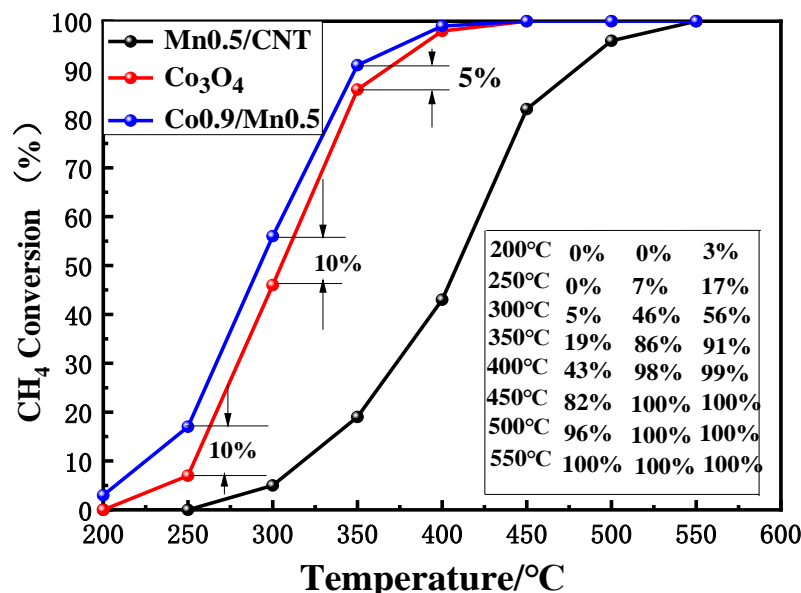


Figure 6. CH_4 conversion, from 200 to 550 °C, of different catalysts.

Recent studies have shown that higher Co^{3+} and higher adsorbed oxygen content are more favorable for lean methane combustion [33]. In our experiment, compared with the Co_3O_4 nano-sheet, doping Mn led to increased values of $\text{Co}^{3+}/\text{Co}^{2+}$ in the Co0.9/Mn0.5 nano-sheet (confirmed by XPS analysis), which increased the mobility of reactive oxygen species, leading to higher catalytic activity. This fact may be the reason why the catalytic activity of the Co0.9/Mn0.5 nano-sheet was higher than that of the Co_3O_4 nano-sheet.

2.4.2. Comprehensive Evaluation of Catalytic Activity of Co0.9/Mn0.5 Catalyst

Next, through simulating the actual situation, the feasibility of the prepared Co0.9/Mn0.5 catalyst in three environments of high temperature conditions (600~900 °C), 450 °C long working time and different methane gas flow rates was validated. Figure 7a shows the catalytic effect of the Co0.9/Mn0.5 nano-sheet catalyst sample at the high temperature condition of 600~900 °C. It was found that the sample did not deactivate at high temperatures, indicating that the sample had the characteristics of high temperature resistance. Next, the stability of the catalyst for a long time at 450 °C was tested. As shown in Figure 7b, the catalytic activity of the catalyst was very stable over 2200 min.

Lastly, the influence of GHSV on catalytic activity was tested in the Co0.9/Mn0.5 nanometer sheet catalyst (Figure 7c). Different methane gas flow rates changed the possibility of contact between methane gas and the catalyst. When the flow rate was too fast, the methane gas may not have reacted completely when leaving the catalyst, which led to a reduction in the removal rate of methane [41]. The fact that methane can still be well burned with a fast flow rate is an important index to evaluate the activity of the catalyst. In order to reduce the influence of error caused by the change in flow velocity, five samples were tested at each flow velocity stage, and the control range of methane flow velocity was $\text{GHSV} = 6000\sim 60,000 \text{ mL}/(\text{g h})$. When the flow rate exceeded $\text{GHSV} = 12,000 \text{ mL}/(\text{g h})$, the catalytic activity decreased. When the flow rate of methane exceeded $\text{GHSV} = 42,000 \text{ mL}/(\text{g h})$, the conversion rate of catalytic methane began to be lower than 90%, indicating that the catalyst had a strong adaptability to the flow rate of methane.

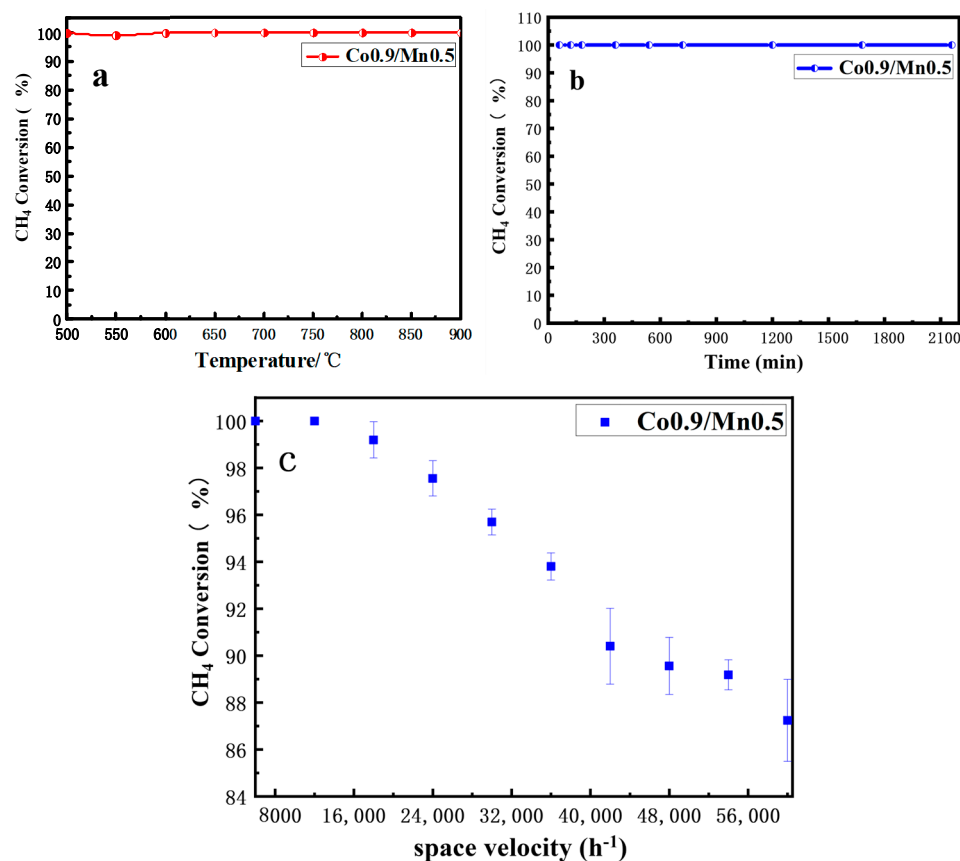


Figure 7. (a) High temperature resistance to sintering test of Co₃O₄ nano-sheet catalyst; (b) thermal stability test of Co₃O₄ nano-sheet catalyst; (c) effect of GHSV on CH₄ conversion over Co₃O₄ nano-sheet catalyst.

2.4.3. The Study of the Catalytic Combustion Kinetics of Low Concentration Methane Gas

The study of the catalytic combustion kinetics of low concentration methane gas can provide the kinetic basis for the establishment of catalytic methane combustion reactor model and further lay the foundation for the development of the technology of low concentration methane gas catalytic combustion to depth direction. In order to better describe the reaction kinetics and reaction series in the methane catalytic process, the kinetic model was introduced and the following methane catalytic combustion reaction rate equation was obtained through the derivation of the formula. The detailed derivation process is given in the supporting information.

By using the vertical axis as $\ln([M^{-1}s^{-1}])$ and the horizontal axis as $1000/T$, the slope obtained, multiplied by R , gives the activation energy E_a . Figure 8 shows the Arrhenius plots of the methane oxidation reaction for the Co₃O₄ nano-sheet and the Mn_{0.5}/CNT and Co_{0.9}/Mn_{0.5} nano-sheet catalysts. Using this formula, within the scope of the 200~325 °C, the activation energy of low concentration methane gas combustion catalyzed by three catalysts was Co_{0.9}/Mn_{0.5} (19.53 kJ·mol⁻¹) < Co₃O₄ (61.72 kJ·mol⁻¹) < Mn_{0.5}/CNT (80.37 kJ·mol⁻¹) from high to low. As can be seen, the activation energies are somewhat lower on the Co_{0.9}/Mn_{0.5} nano-sheet catalysts, indicating that the addition of Mn₃O₄ especially lowered the methane activation barrier [42].

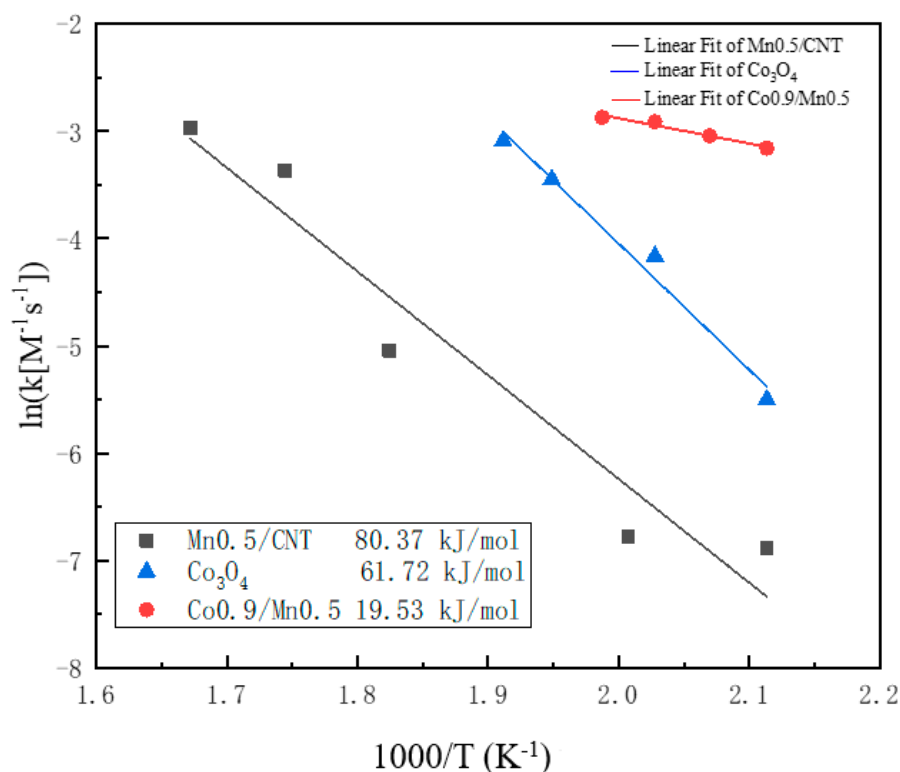


Figure 8. Arrhenius-type plots for methane oxidation of Co₃O₄ nano-sheet, Mn_{0.5}/CNT and Co_{0.9}/Mn_{0.5} nano-sheet.

3. Discussion

3.1. The Interaction of Co₃O₄ and Mn₃O₄

In order to better understand the influence of Mn₃O₄ dopant on the catalytic performance of a Co₃O₄ nano-sheet catalyst, XPS analysis was performed. XPS analysis was used to determine the influence of Mn₃O₄ doping on the surface chemical state of Co₃O₄ before and after doping.

Figure 9 shows the XPS spectra of O 1s, C 1s, Co 2p and Mn 2p_{1/2} on the surface of the Co₃O₄ nano-sheet, MnO₂/CNT and Co_{0.9}/Mn_{0.5} nano-sheet catalysts. For O 1s (Figure 9a,b), the peak at 530.3 eV corresponds to lattice oxygen (O_I), while the peak at 531.6 eV corresponds to adsorbed oxygen (O_{II}) [43]. By observing Figure 9a,b, it can be found that the O_{II}/O_I of the Co_{0.9}/Mn_{0.5} sample was higher than that of the Co₃O₄ nano-sheet sample, while the MnO₂/CNT sample had more pollutants and adsorbed water. The specific data are shown in Table 3, where O_I and O_{II} were calculated based on the quantitative analysis of the O 1s spectrum, which is attributed to the entry of manganese ions into the lattice of Co₃O₄. Because the mobility of O_{II} is stronger than O_I, the oxidation ability of O_{II} to methane is stronger than O_I, and more O_{II} can generate more oxygen vacancy to improve the catalytic combustion efficiency of methane [44]. The different atomic percentages of the MnO₂/CNT and Co₃O₄/Mn₃O₄ nano-sheets on the catalyst surface, and their corresponding positions, are given in Table 3. The variation trend of atomic percentages on the catalyst surface was consistent with that of manganese salt and cobalt salt concentration, which is well consistent with Figure S6. The specific value is shown in Table 4. The O_{II}/O_I of the Co₃O₄/Mn₃O₄ catalyst were higher than that of Co₃O₄, indicating that the intervention of manganese could change the O_{II}/O_I of Co₃O₄.

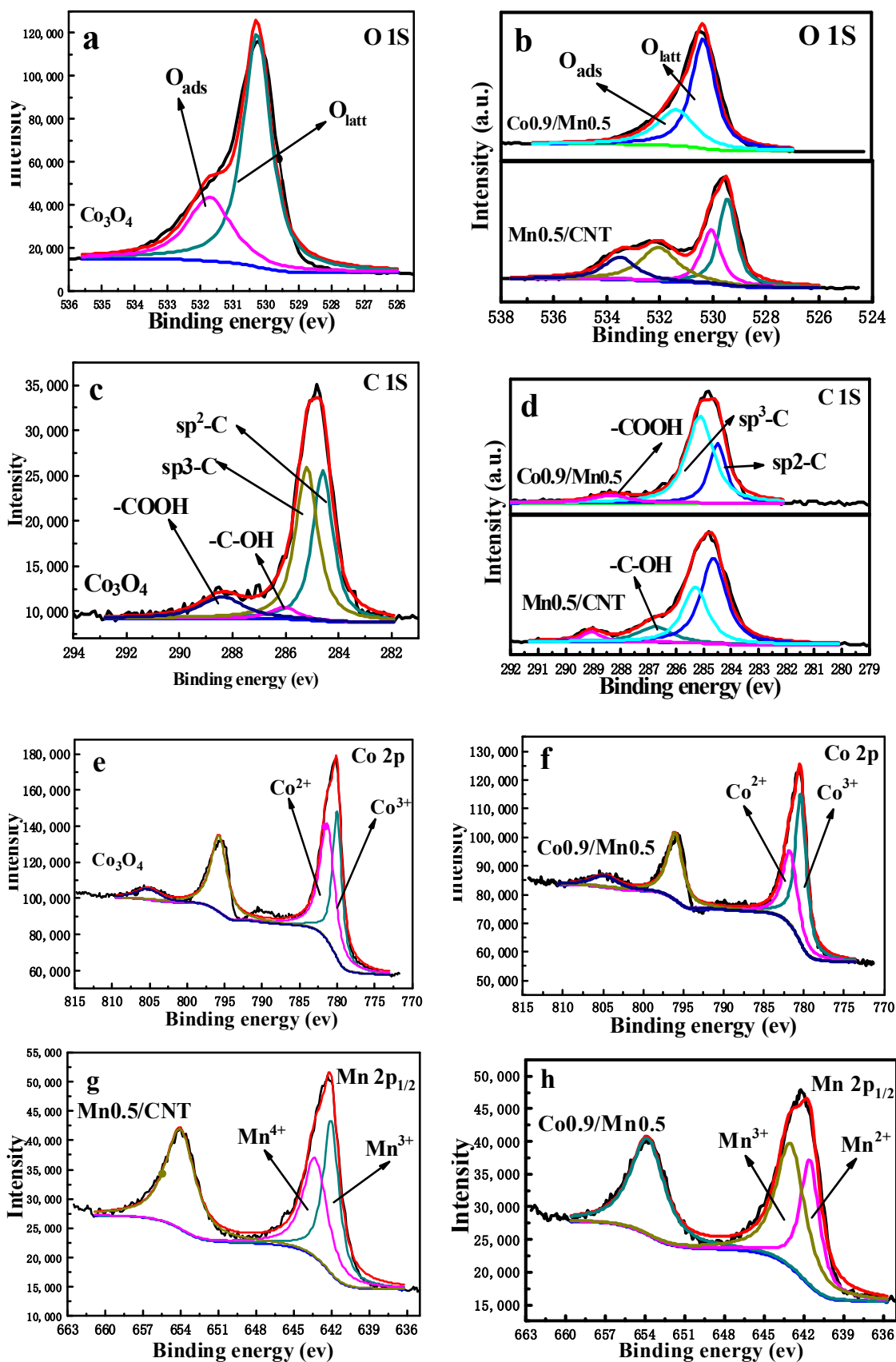


Figure 9. XPS spectra acquired of Co₃O₄ nano-sheet, Mn_{0.5}/CNT and Co_{0.9}/Mn_{0.5} nano-sheet: (a,b) O1s, (c,d) C1s, (e,f) Co2p and (g,h) Mn 2p_{1/2}.

Table 3. XPS results of MnO₂/CNT and Co₃O₄/Mn₃O₄ catalysts (surface atomic composition (%), peak position (eV)).

Sample	Surface Atomic Composition (%)				Peak Position (eV)			
	Mn	Co	O	C	Mn 2p _{1/2}	Mn 2p _{3/2}	Co 2p _{1/2}	Co 2p _{3/2}
Mn0.3/CNT	8.35	0.0	22.46	69.19	653.9	642.4	-	-
Mn0.5/CNT	8.77	0.0	29.35	61.88	654.0	642.3	-	-
Mn0.7/CNT	16.58	0.0	39.8	43.62	654.3	642.6	-	-
Co0.1/Mn0.5	13.03	2.92	34.97	49.07	653.5	642.2	796.0	780.7
Co0.5/Mn0.5	8.98	7.68	36.8	46.53	653.9	642.0	795.8	780.5
Co0.9/Mn0.5	8.28	11.69	43.27	36.76	654.0	642.0	795.8	780.6
Co ₃ O ₄	-	20.85	47.83	31.32	-	-	795.5	780.3

Table 4. XPS results of MnO₂/CNT and Co₃O₄/Mn₃O₄ catalysts (O_{II}/O_I, Co³⁺/Co²⁺, Mn⁴⁺/Mn³⁺, Mn³⁺/Mn²⁺).

Sample	O _{II} /O _I	Co ³⁺ /Co ²⁺	Mn ⁴⁺ /Mn ³⁺	Mn ³⁺ /Mn ²⁺
Mn0.3/CNT	0.64	-	0.96	-
Mn0.5/CNT	0.69	-	0.93	-
Mn0.7/CNT	0.65	-	0.86	-
Co0.1/Mn0.5	0.67	0.98	-	1.18
Co0.5/Mn0.5	0.72	1.30	-	1.27
Co0.9/Mn0.5	0.89	1.55	-	1.46
Co ₃ O ₄	0.60	0.79	-	-

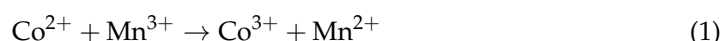
The high-resolution C 1s spectra of CNTs are shown in Figure 9c,d, in order to verify the variation of the edge carbon density. As can be seen, four components can be deconvoluted, corresponding to the sp²-hybridized carbon (284.6 eV), sp³-hybridized carbon (285.3 eV), -C-OH (286.1 eV) and -COOH (288.4 eV), respectively [32]. Since the degree of oxidation of CNTs in the three catalysts was different, there was a significant difference in the relative content of sp³-hybridized carbon on the surface of the three catalysts. The relative content of sp³-hybridized carbon on the surface of the Co0.9/Mn0.5 nano-sheet was the highest, indicating that CNTs were most oxidized. Observing the C 1S spectrum of the MnO₂/CNT and Mn₃O₄/Co₃O₄ nano-sheets catalysts in Figure 9c,d, the relative content of sp³-hybridized carbon still had a regular change, that is, the higher the catalytic activity of the catalyst, the more obvious the sp³-hybridization.

In Figure 9e,f, the shape and position of the spectral lines of the Co₃O₄ and Co0.9/Mn0.5 nano-sheet catalysts are all typical spinel structures. The peaks at 780.2 ± 0.2 and 782.2 ± 0.2 eV correspond to Co³⁺ and Co²⁺, respectively, and the small peaks at 789.4 eV belong to the vibration satellite peak of Co²⁺ [45]. In comparison with Figure 9e,f, the ratio of Co³⁺/Co²⁺ in the Co0.9/Mn0.5 nano-sheet sample was higher than that of the undoped Mn₃O₄ nano-sheet sample, and the specific data are shown in Table 3. As analyzed by XRD and TEM, Mn³⁺ replaces the Co³⁺ partially located in the octahedron, resulting in lattice expansion. According to the Jahn–Teller effect, the replacement of Mn³⁺ in the octahedron will cause local tetragonal distortion, so the Mn³⁺ occupying the octahedron is not stable and the Co²⁺ near Mn³⁺ will show a trend of transformation to Co³⁺ [33,37]. In the process of conversion from Co²⁺ to Co³⁺, the oxygen vacancy [46] content and oxygen species mobility could be improved, so the catalytic activity of the Co0.9/Mn0.5 catalyst was higher. At the same time, the relative content of Co³⁺/Co²⁺ on the surface of the Co₃O₄/Mn₃O₄ nano-sheet catalyst with different cobalt-manganese ratios is shown in Figure S9, and the specific data are shown in Table 4. The Co³⁺/Co²⁺ values of the Co₃O₄/Mn₃O₄ nano-sheet catalysts with different cobalt-manganese ratios were all higher than those of the Co₃O₄ nano-sheet catalysts, further indicating that manganese doping can change the relative content of different cobalt valence states.

Figure 9g,h are the Mn 2p_{1/2} XPS spectra of Mn0.5/CNT and Co0.9/Mn0.5, respectively. The valence states of Mn in the two samples were different. The Mn⁴⁺ and Mn³⁺ in the Mn0.5/CNT sample corresponded to 643.4eV and 642eV, respectively (Figure 9g) [45,47], and the Mn²⁺ and Mn³⁺ in the Co0.9/Mn0.5 sample corresponded to 641.6 eV and 643.1 eV, respectively (Figure 9h) [48]. On the surface of the Co0.9/Mn0.5 catalyst, Mn²⁺ and Mn³⁺ could combine with Co²⁺ to form redox pairs of Co²⁺-O²⁻-Mn³⁺, improving the oxygen mobility of the catalyst [35]. In Figure S10, the Mn³⁺/Mn²⁺ value was also observed to be proportional to the proportion of cobalt and manganese. The Mn³⁺/Mn²⁺ value of the Co₃O₄/Mn₃O₄ catalyst is given in Table 4, and the Mn³⁺/Mn²⁺ value of Co0.9/Mn0.5 is the largest. According to the catalytic effect, the catalytic activity increases with the increase in Mn³⁺ ion content.

3.2. Analysis of the Mechanism of Mn₃O₄ Promoting the Catalytic Oxidation of Methane by Co₃O₄

The characterization analysis shows that the interaction between Mn ions and Mn₃O₄ led to lattice distortion in Co₃O₄. Specifically, the participation of Mn²⁺ promoted the transformation of Co²⁺ to Co³⁺, but oxygen vacancies needed to be replenished during the process. The lack of oxygen vacancies could be provided by the transformation of Mn³⁺ to Mn²⁺, indicating that Co²⁺ → Co³⁺ and Mn³⁺ → Mn²⁺ occurred simultaneously. During the transformation of Co²⁺ → Co³⁺ or Co³⁺ → Co²⁺, a large number of oxygen vacancy defects appeared, effectively adsorbing O₂ in methane gas and converting it to lattice oxygen (O_I) [1,49]. At the same time, some O_{II} was used for the further oxidation of Co²⁺ and Mn²⁺. This also explains why the relative content of O_{II} in Co0.9/Mn0.5 was higher than that in Co₃O₄. Therefore, it can be concluded that the promotion mechanism of Mn ions was mainly achieved by inducing lattice distortion in Co₃O₄. In the catalytic oxidation process of methane, the oxygen reduction reaction of Mn³⁺/Mn²⁺ played a role in buffering the oxygen transport and storage. The oxygen reduction reaction of Co³⁺/Co²⁺ played a role in transferring oxygen to the catalyst surface and the oxygen vacancies could supplement oxygen molecules in the methane mixture to generate active oxygen. In summary, the promotion mechanism of Mn₃O₄ on the catalytic oxidation of methane by Co₃O₄ in Figure 10 can be more comprehensively explained and understood by capturing oxygen molecules in the methane mixture to supplement oxygen vacancies and further form active oxygen. The method is as follows [33,35,37]:



Under the interaction of Mn₃O₄ and Co₃O₄, the formation of reactive oxygen species can be accelerated by enhancing the oxygen mobility on the catalyst surface (*_□ represents catalyst active center, O* represents oxygen vacancy).

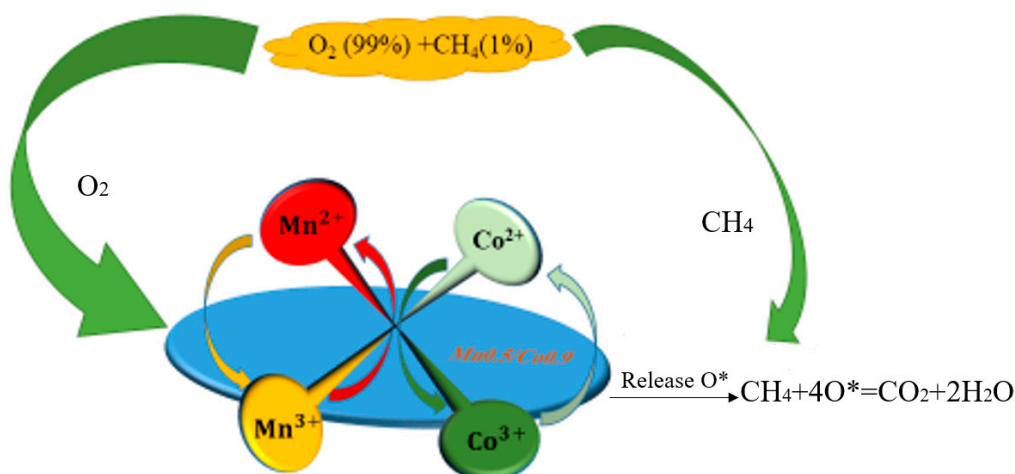


Figure 10. The mechanism of Mn_3O_4 promoting the catalytic oxidation of CH_4 by Co_3O_4 (O^* represents oxygen vacancy).

4. Materials and Methods

4.1. Preparation of Catalysts

Preparation of Co_3O_4 nano-sheet: Co_3O_4 nano-sheets were prepared using the hard template method. An amount of 0.9 M cobalt nitrate solution of 25 mL was prepared. A total of 0.15 g CNT (Manufactured by Shenzhen Guoheng Qihang Technology Co., Ltd., Shenzhen, China) was immersed in $\text{Co}(\text{NO}_3)_2 \cdot 6\text{H}_2\text{O}$ solution and boiled at 100 °C for 1 h. The cobalt nitrate solution was then adsorbed and left overnight. Finally, they were blown dried under 80 °C for 6 h, and annealed under 400 °C for 3 h.

Preparation of MnO_2/CNT and $\text{Co}_3\text{O}_4/\text{Mn}_3\text{O}_4$: MnO_2/CNT and two-dimensional $\text{Co}_3\text{O}_4/\text{Mn}_3\text{O}_4$ nano-sheets were prepared using the hard template method. As is typical, 25 mL composite solution of manganese nitrate solution and manganese nitrate cobalt was prepared. Then, 0.15 g CNT was weighed and soaked in the above solution and boiled for 1 h at 100 °C. The solution was then sucked out and left overnight. Finally, they were blown dried under 80 °C for 6 h, and annealed under 400 °C for 3 h. In the process of preparing MnO_2/CNT , the catalysts prepared by manganese nitrate solutions with different concentrations were expressed by MnX/CNT , where X represented manganese nitrate solutions with concentrations of 0.3 M, 0.5 M and 0.7 M. In the preparation of two-dimensional $\text{Co}_3\text{O}_4/\text{Mn}_3\text{O}_4$ nano-sheet, $\text{CoY}/\text{Mn0.5}$, Mn0.5 represents manganese nitrate solution with a solubility of 0.5 M, and Y represents $\text{Co}(\text{NO}_3)_2 \cdot 6\text{H}_2\text{O}$ solution with a concentration of 0.1 M, 0.5 M and 0.9 M.

4.2. Catalyst Characterization

Morphological and microstructure analyses of the different types of catalysts were performed using a scanning electron microscope (SEM; ZEISS SUPRA-55, Zeiss, Munich, Germany) at an acceleration voltage of 5 kV. The phase composition was analyzed utilizing a powder X-ray diffraction system with $\text{Cu K}\alpha$ radiation (XRD; DX2500 Dandong Fangyuan, Dandong, China). The specific surface areas (SSA), the pore size distribution (PSD) and pore volume were determined by specific surface area analyzer (SSA; SSA-4000 Biaode, Lanzhou, China). TG was analyzed by thermal gravimetric analyzer (TG; HCT-2 Beijing Hengjiu Scientific Instrument Factory, Beijing, China). Surface chemical state analysis of the different types of catalysts was characterized by X-ray photoelectron spectroscopy (XPS; ESCALAB250 Thermo VG, Waltham, MA, USA). The charging effect was corrected by referencing the binding energy of C 1 s at 284.6 eV.

4.3. Catalytic Performance Measurements

The catalytic performance for CH_4 combustion was tested in a fixed-bed quartz reactor (i.d.4 mm) packed with 0.1 g catalyst. The reaction temperature was controlled by intelligent

temperature regulator. The low concentration methane gas, containing 0.1 vol.% CH₄ in air, was supplied to the catalyst bed through a mass flow controller at a gas hourly space velocity (GHSV) of 6000 mL·g⁻¹·h⁻¹. The gas compositions were also analyzed by a GC-7890 gas chromatograph equipped with FID and TCD detectors, the model of the activity evaluation device is shown in Figure S1. The conversion of CH₄ was calculated using the following formula:

$$X(\%) = (C_{\text{in}} - C_{\text{out}}) / C_{\text{in}} \times 100\% \quad (5)$$

where X presents the CH₄ conversion, C_{in} stands for the initial CH₄ concentration in the inlet and C_{out} stands for the CH₄ concentration in the outlet.

5. Conclusions

In this work, for the first time, a two-dimensional Co₃O₄ nano-sheet catalyst was successfully prepared using CNT as a hard template. The two dimensional Co_{0.9}/Mn_{0.5} composite catalyst with higher catalytic activity was prepared by doping Mn₃O₄. During the preparation of the Co₃O₄ nano-sheet, the thermal stability of CNT and the structural changes of Co₃O₄ were further understood by controlling the air burning time. The microstructure characterization and surface chemical states of the three types of catalysts proved that the high catalytic activity of the Co_{0.9}/Mn_{0.5} catalyst was mainly attributed to the following reasons: (1) the interference of Mn³⁺ causes lattice distortion of Co₃O₄ and reduces the agglomeration degree of the catalyst. (2) The regular arrangement of atoms on the surface of the exposed crystal face is one of the important reasons for the high catalytic activity. (3) The interaction between Mn and Co promotes the cycle capacity of Mn/Co redox pairs and produces more species of reactive oxygen species. By comparing the activation energy of methane gas combustion catalyzed by three catalysts, it can be found that the Co_{0.9}/Mn_{0.5} catalyst with high catalytic activity can significantly reduce the activation energy of methane combustion. Meanwhile, the catalytic activity of the Co_{0.9}/Mn_{0.5} catalyst remained stable under different catalytic conditions.

Supplementary Materials: The following supporting information can be downloaded at: <https://www.mdpi.com/article/10.3390/catal13071112/s1>, Figure S1: Schematic diagram of the experimental set-up; Figure S2: SEM images of Co₃O₄ nano-sheet prepared at annealing times of 3 and 10 min; Figure S3: XRD patterns of Co₃O₄ nano-sheet prepared at different annealing times, and JCPDS card is from ref. 50; Figure S4: CH₄ conversion from 200 to 550 °C over (A) MnO₂/CNT and (B) Co₃O₄/Mn₃O₄ catalysts; Figure S5: SEM images of MnO₂/CNT and Co₃O₄/Mn₃O₄ catalysts; Figure S6: EDS images of MnO₂/CNT and Co₃O₄/Mn₃O₄ catalysts; Figure S7: XRD patterns of MnO₂/CNT and Co₃O₄/Mn₃O₄ catalysts; Figure S8: Pore size distributions of MnO₂/CNT (a) and Co₃O₄/Mn₃O₄ catalysts (b); Figure S9: XPS spectra of Co³⁺/Co²⁺ on the surface of Co₃O₄/Mn₃O₄ nano-sheet catalyst with different cobalt-manganese ratios; Figure S10: XPS spectra of Mn³⁺/Mn²⁺ on the surface of Co₃O₄/Mn₃O₄ nano-sheet catalyst with different cobalt-manganese ratios; Figure S11: XPS spectra of Co₃O₄ and Co_{0.9}/Mn_{0.5} nano-catalysts; Table S1: Pore parameters of the materials; Table S2: Crystal face index, full width at half maximum, and grain size of CNT and Co₃O₄ nano-sheet catalysts prepared at different annealing times at 1 min, 6 min, 30 min, and 60 min [50].

Author Contributions: Conceptualization: X.W., J.Q. and H.W.; methodology, validation, formal analysis and investigation: X.W., K.Y., Q.Z. and J.L.; resources: H.W.; data curation: H.W.; writing—original draft preparation: X.W., K.Y., Q.Z. and J.L.; writing—review and editing: J.Q. and H.W.; visualization: H.W.; supervision: H.W.; project administration: H.W.; funding acquisition: H.W.; All authors have read and agreed to the published version of the manuscript.

Funding: This work was supported by the Natural Science Foundation of China under Grant (No. 21604007, H.W.).

Data Availability Statement: Not applicable.

Conflicts of Interest: The authors declare no conflict of interest.

References

1. Hu, W.; Lan, J.; Guo, Y.; Cao, X.-M.; Hu, P. Origin of efficient catalytic combustion of methane over Co_3O_4 (110): Active low-coordination lattice oxygen and cooperation of multiple active sites. *ACS Catal.* **2016**, *6*, 5508–5519. [[CrossRef](#)]
2. Wang, Q.; Peng, Y.; Fu, J.; Kyzas, G.Z.; Billah, S.M.R.; An, S.Q. Synthesis, characterization, and catalytic evaluation of $\text{Co}_3\text{O}_4/\text{gamma-Al}_2\text{O}_3$ as methane combustion catalysts: Significance of Co species and the redox cycle. *Appl. Catal. B Environ.* **2015**, *168*, 42–50. [[CrossRef](#)]
3. Zavyalova, U.; Scholz, P.; Ondruschka, B. Influence of cobalt precursor and fuels on the performance of combustion synthesized $\text{Co}_3\text{O}_4/\text{gamma-Al}_2\text{O}_3$ catalysts for total oxidation of methane. *Appl. Catal. A Gen.* **2007**, *323*, 226–233. [[CrossRef](#)]
4. Pu, Z.Y.; Zhou, H.; Zheng, Y.F.; Huang, W.Z.; Li, X.N. Enhanced methane combustion over Co_3O_4 catalysts prepared by a facile precipitation method: Effect of aging time. *Appl. Surf. Sci.* **2017**, *410*, 14–21. [[CrossRef](#)]
5. Yang, J.; Lee, J.Y.; Ying, J.Y. Phase transfer and its applications in nanotechnology. *Chem. Soc. Rev.* **2011**, *40*, 1672–1696. [[CrossRef](#)] [[PubMed](#)]
6. Zhang, W.D.; Wu, F.; Li, J.J.; You, Z.X. Dispersion-precipitation synthesis of highly active nanosized Co_3O_4 for catalytic oxidation of carbon monoxide and propane. *Appl. Surf. Sci.* **2017**, *411*, 136–143. [[CrossRef](#)]
7. Chen, Y.T.; Wang, S.; Chen, Z.P.; Ding, Y.; Zhang, L.; Lv, L.R.; Wang, Y.; Xu, D.K.; Wang, S.D. Synthesis of Co_3O_4 nanosheets with controllable size and their catalytic property. *Solid State Sci.* **2018**, *82*, 78–83. [[CrossRef](#)]
8. Wang, K.; Cao, Y.L.; Hu, J.D.; Li, Y.Z.; Xie, J.; Jia, D.Z. Solvent-Free Chemical Approach to Synthesize Various Morphological Co_3O_4 for CO Oxidation. *ACS Appl. Mater. Interfaces* **2017**, *9*, 16128–16137. [[CrossRef](#)]
9. Meng, B.; Zhao, Z.B.; Wang, X.Z.; Liang, J.J.; Qiu, J.S. Selective catalytic reduction of nitrogen oxides by ammonia over Co_3O_4 nanocrystals with different shapes. *Appl. Catal. B Environ.* **2013**, *129*, 491–500. [[CrossRef](#)]
10. Chen, Z.P.; Wang, S.; Liu, W.G.; Gao, X.H.; Gao, D.N.; Wang, M.Z.; Wang, S.D. Morphology-dependent performance of Co_3O_4 via facile and controllable synthesis for methane combustion. *Appl. Catal. A Gen.* **2016**, *525*, 94–102. [[CrossRef](#)]
11. Xie, X.W.; Li, Y.; Liu, Z.Q.; Haruta, M.; Shen, W.J. Low-temperature oxidation of CO catalysed by Co_3O_4 nanorods. *Nature* **2009**, *458*, 746–749. [[CrossRef](#)]
12. Khasu, M.; Nyathi, T.; Morgan, D.J.; Hutchings, G.J.; Claeys, M.; Fischer, N. Co_3O_4 morphology in the preferential oxidation of CO. *Catal. Sci. Technol.* **2017**, *7*, 4806–4817. [[CrossRef](#)]
13. Giovannelli, F.; Marsteau, V.; Zaghrioui, M.; Autret, C.; Delorme, F. Low temperature synthesis of Co_3O_4 and $(\text{Co}_{1-x}\text{Mn}_x)_3\text{O}_4$ spinels nanosheets. *Adv. Powder Technol.* **2017**, *28*, 1325–1331. [[CrossRef](#)]
14. Cai, Y.; Xu, J.; Guo, Y.; Liu, J. Ultrathin, polycrystalline, two-dimensional Co_3O_4 for low-temperature CO oxidation. *ACS Catal.* **2019**, *9*, 2558–2567. [[CrossRef](#)]
15. Wang, F.; Zhang, L.; Xu, L.; Deng, Z.; Shi, W. Low temperature CO oxidation and CH_4 combustion over Co_3O_4 nanosheets. *Fuel* **2017**, *203*, 419–429. [[CrossRef](#)]
16. Li, P.; Chen, X.; Ma, L.; Bhat, A.; Li, Y.; Schwank, J.W. Effect of Ce and La dopants in Co_3O_4 nanorods on the catalytic activity of CO and C_3H_6 oxidation. *Catal. Sci. Technol.* **2019**, *9*, 1165–1177. [[CrossRef](#)]
17. Yang, J.; Ying, J.Y. Nanocomposites of Ag_2S and noble metals. *Angew. Chem. Int. Ed.* **2011**, *50*, 4637–4643. [[CrossRef](#)]
18. Zarnegar, Z.; Safari, J.; Kafroudi, Z.M. Co_3O_4 -CNT nanocomposites: A powerful, reusable, and stable catalyst for sonochemical synthesis of polyhydroquinolines. *New J. Chem.* **2015**, *39*, 1445–1451. [[CrossRef](#)]
19. Zarnegar, Z.; Safari, J.; Mansouri-Kafroudi, Z. Environmentally benign synthesis of polyhydroquinolines by Co_3O_4 -CNT as an efficient heterogeneous catalyst. *Catal. Commun.* **2015**, *59*, 216–221. [[CrossRef](#)]
20. Kuo, C.-H.; Li, W.; Song, W.; Luo, Z.; Poyraz, A.S.; Guo, Y.; Ma, A.W.; Suib, S.L.; He, J. Facile synthesis of Co_3O_4 @CNT with high catalytic activity for CO oxidation under moisture-rich conditions. *ACS Appl. Mater. Interfaces* **2014**, *6*, 11311–11317. [[CrossRef](#)]
21. Chen, H.; Wang, W.; Yang, L.; Dong, L.; Wang, D.; Xu, X.; Wang, D.; Huang, J.; Lv, M.; Wang, H. A review of cobalt-containing nanomaterials, carbon nanomaterials and their composites in preparation methods and application. *Nanomaterials* **2022**, *12*, 2042. [[CrossRef](#)]
22. Yang, L.; Zhu, Q.; Yang, K.; Xu, X.; Huang, J.; Chen, H.; Wang, H. A Review on the Application of Cobalt-Based Nanomaterials in Supercapacitors. *Nanomaterials* **2022**, *12*, 4065. [[CrossRef](#)] [[PubMed](#)]
23. Wu, Z.; Zhao, Y.; Chen, X.; Guo, Y.; Wang, H.; Jin, Y.; He, P.; Wei, Q.; Wang, B. Preparation of polymeric carbon nitride/ TiO_2 heterostructure with NH_4Cl as template: Structural and photocatalytic studies. *J. Phys. Chem. Solids* **2022**, *164*, 110629. [[CrossRef](#)]
24. Zhou, J.; Song, H.; Chen, X.; Huo, J. Diffusion of metal in a confined nanospace of carbon nanotubes induced by air oxidation. *J. Am. Chem. Soc.* **2010**, *132*, 11402–11405. [[CrossRef](#)] [[PubMed](#)]
25. Wang, X.; Zhao, H.; Chang, L.; Yu, Z.; Xiao, Z.; Tang, S.; Huang, C.; Fan, J.; Yang, S. First-Principles Study on Interlayer Spacing and Structure Stability of NiAl-Layered Double Hydroxides. *ACS Omega* **2022**, *7*, 39169–39180. [[CrossRef](#)] [[PubMed](#)]
26. Thissen, N.F.; Verheijen, M.; Houben, R.; Van Der Marel, C.; Kessels, W.; Bol, A. Synthesis of single-walled carbon nanotubes from atomic-layer-deposited Co_3O_4 and $\text{Co}_3\text{O}_4/\text{Fe}_2\text{O}_3$ catalyst films. *Carbon* **2017**, *121*, 389–398. [[CrossRef](#)]
27. Fu, W.; Zhao, Y.; Wang, H.; Chen, X.; Liu, K.; Zhang, K.; Wei, Q.; Wang, B. Study on preparation, photocatalytic performance and degradation mechanism of polymeric carbon nitride/Pt/nano-spherical MoS_2 composite. *J. Phys. Chem. Solids* **2022**, *166*, 110700. [[CrossRef](#)]
28. Xiong, X.; Jin, Y.; Wang, H.; He, P.; Xiang, X.; Hu, P.; Liu, K.; Wei, Q.; Wang, B. Study on the hydrogen production properties and electron transfer mechanism of CdS/WO_3 composite photocatalyst. *Mater. Chem. Phys.* **2022**, *281*, 125824. [[CrossRef](#)]

29. Wang, X.; Zhang, J.; Yang, S.; Yan, H.; Hong, X.; Dong, W.; Liu, Y.; Zhang, B.; Wen, Z. Interlayer space regulating of NiMn layered double hydroxides for supercapacitors by controlling hydrothermal reaction time. *Electrochim. Acta* **2019**, *295*, 1–6. [[CrossRef](#)]
30. Wang, X.; Yan, H.; Zhang, J.; Hong, X.; Yang, S.; Wang, C.; Li, Z. Stamen-petal-like CeO₂/NiMn layered double hydroxides composite for high-rate-performance supercapacitor. *J. Alloys Compd.* **2019**, *810*, 151911. [[CrossRef](#)]
31. Wang, X.; Wu, F.; Fan, J.; Tian, A.; Cheng, Y.; Yang, S. High specific surface area NiTiAl layered double hydroxide derived via alkali etching for high performance supercapacitor electrode. *J. Alloys Compd.* **2021**, *888*, 161502. [[CrossRef](#)]
32. Cao, Y.; Li, B.; Zhong, G.; Li, Y.; Wang, H.; Yu, H.; Peng, F. Catalytic wet air oxidation of phenol over carbon nanotubes: Synergistic effect of carboxyl groups and edge carbons. *Carbon* **2018**, *133*, 464–473. [[CrossRef](#)]
33. Zhao, W.; Zhang, Y.; Wu, X.; Zhan, Y.; Wang, X.; Au, C.-T.; Jiang, L. Synthesis of Co–Mn oxides with double-shelled nanocages for low-temperature toluene combustion. *Catal. Sci. Technol.* **2018**, *8*, 4494–4502. [[CrossRef](#)]
34. Li, J.; Liang, X.; Xu, S.; Hao, J. Catalytic performance of manganese cobalt oxides on methane combustion at low temperature. *Appl. Catal. B Environ.* **2009**, *90*, 307–312. [[CrossRef](#)]
35. Chang, T.; Shen, Z.; Huang, Y.; Lu, J.; Ren, D.; Sun, J.; Cao, J.; Liu, H. Post-plasma-catalytic removal of toluene using MnO₂–Co₃O₄ catalysts and their synergistic mechanism. *Chem. Eng. J.* **2018**, *348*, 15–25. [[CrossRef](#)]
36. Piumetti, M.; Fino, D.; Russo, N. Mesoporous manganese oxides prepared by solution combustion synthesis as catalysts for the total oxidation of VOCs. *Appl. Catal. B Environ.* **2015**, *163*, 277–287. [[CrossRef](#)]
37. Wang, B.; Chi, C.; Xu, M.; Wang, C.; Meng, D. Plasma-catalytic removal of toluene over CeO₂–MnO_x catalysts in an atmosphere dielectric barrier discharge. *Chem. Eng. J.* **2017**, *322*, 679–692. [[CrossRef](#)]
38. Shi, C.; Wang, Y.; Zhu, A.; Chen, B.; Au, C. Mn_xCo_{3–x}O₄ solid solution as high-efficient catalysts for low-temperature oxidation of formaldehyde. *Catal. Commun.* **2012**, *28*, 18–22. [[CrossRef](#)]
39. El-Shobaky, H.G.; Shouman, M.A.; Attia, A.A. Effect of La₂O₃ and Mn₂O₃-doping of Co₃O₄/Al₂O₃ system on its surface and catalytic properties. *Colloids Surf. A Physicochem. Eng. Asp.* **2006**, *274*, 62–70. [[CrossRef](#)]
40. Laugel, G.; Arichi, J.; Guerba, H.; Moliere, M.; Kiennemann, A.; Garin, F.; Louis, B. Co₃O₄ and Mn₃O₄ Nanosheets Dispersed on SBA-15: Efficient Catalysts for Methane Combustion. *Catal. Lett.* **2008**, *125*, 14–21. [[CrossRef](#)]
41. Wang, L.-C.; Huang, X.-S.; Liu, Q.; Liu, Y.-M.; Cao, Y.; He, H.-Y.; Fan, K.-N.; Zhuang, J.-H. Gold nanosheets deposited on manganese (III) oxide as novel efficient catalyst for low temperature CO oxidation. *J. Catal.* **2008**, *259*, 66–74. [[CrossRef](#)]
42. Okal, J.; Zawadzki, M.; Baranowska, K. Methane combustion over bimetallic Ru-Re/ γ -Al₂O₃ catalysts: Effect of Re and pretreatments. *Appl. Catal. B Environ.* **2016**, *194*, 22–31. [[CrossRef](#)]
43. Sutthumporn, K.; Kawi, S. Promotional effect of alkaline earth over Ni–La₂O₃ catalyst for CO₂ reforming of CH₄: Role of surface oxygen species on H₂ production and carbon suppression. *Int. J. Hydrogen Energy* **2011**, *36*, 14435–14446. [[CrossRef](#)]
44. Qu, R.; Gao, X.; Cen, K.; Li, J. Relationship between structure and performance of a novel cerium-niobium binary oxide catalyst for selective catalytic reduction of NO with NH₃. *Appl. Catal. B Environ.* **2013**, *142*, 290–297. [[CrossRef](#)]
45. Tang, X.; Gao, F.; Xiang, Y.; Yi, H.; Zhao, S. Low temperature catalytic oxidation of nitric oxide over the Mn–CoO_x catalyst modified by nonthermal plasma. *Catal. Commun.* **2015**, *64*, 12–17. [[CrossRef](#)]
46. Wang, Y.; Oord, R.; Van Den Berg, D.; Weckhuysen, B.M.; Makkee, M. Oxygen vacancies in reduced Rh/and Pt/ceria for highly selective and reactive reduction of NO into N₂ in excess of O₂. *ChemCatChem* **2017**, *9*, 2935–2938. [[CrossRef](#)]
47. Wu, M.; Zhan, W.; Guo, Y.; Guo, Y.; Wang, Y.; Wang, L.; Lu, G. An effective Mn–Co mixed oxide catalyst for the solvent-free selective oxidation of cyclohexane with molecular oxygen. *Appl. Catal. A Gen.* **2016**, *523*, 97–106. [[CrossRef](#)]
48. Li, D.; Yang, G.; Li, P.; Wang, J.; Zhang, P. Promotion of formaldehyde oxidation over Ag catalyst by Fe doped MnO_x support at room temperature. *Catal. Today* **2016**, *277*, 257–265. [[CrossRef](#)]
49. Zhu, X.; Liu, S.; Cai, Y.; Gao, X.; Zhou, J.; Zheng, C.; Tu, X. Post-plasma catalytic removal of methanol over Mn–Ce catalysts in an atmospheric dielectric barrier discharge. *Appl. Catal. B Environ.* **2016**, *183*, 124–132. [[CrossRef](#)]
50. Wang, H.; Mao, D.; Qi, J.; Zhang, Q.; Ma, X.; Song, S.; Gu, L.; Yu, R.; Wang, D. Hollow Multishelled Structure of Heterogeneous Co₃O₄–CeO_{2–x} Nanocomposite for CO Catalytic Oxidation. *Adv. Funct. Mater.* **2019**, *29*, 1806588. [[CrossRef](#)]

Disclaimer/Publisher’s Note: The statements, opinions and data contained in all publications are solely those of the individual author(s) and contributor(s) and not of MDPI and/or the editor(s). MDPI and/or the editor(s) disclaim responsibility for any injury to people or property resulting from any ideas, methods, instructions or products referred to in the content.